RSC Advances

PAPER

View Article Online
View Journal | View Issue

Cite this: *RSC Adv.*, 2018, **8**, 25283

New insights into the effect of morphology on catalytic properties of MnO_x–CeO_2 mixed oxides for chlorobenzene degradation

Zhiming Li,† Xiaolin Guo,† Fei Tao and Renxian Zhou *

Received 11th May 2018
Accepted 22nd June 2018

DOI: 10.1039/c8ra04010a

rsc.li/rsc-advances

We synthesized four CeO_2–MnO_x mixed oxides with different morphologies using simple hydrothermal methods. The catalytic activity for chlorobenzene (CB) degradation decreases in the following order: rod-CeO_2–MnO_x > plate-CeO_2–MnO_x > polyhedra-CeO_2–MnO_x > cube-CeO_2–MnO_x. CeO_2 and MnO_x in the mixed oxides are highly dispersed and two new phases of both todorokite (S.G.: *P*2/*m*:*b*) and vernadite (S.G.: *I*4/*m*) with a special tunnel-like structure are found. Both rod-CeO_2–MnO_x and plate-CeO_2–MnO_x exhibit increased lattice microstrains generated from lattice distortion and defects; further, there are more oxygen vacancies and more MnO_x (Mn^{4+} and Mn^{2+}) species on the surface, particularly when compared to cube-CeO_2–MnO_x. Therefore, this promotes deeper oxidation activity for CB. Moreover, the strong interaction between CeO_2 and MnO_x also promotes the redox ability of CeO_2–MnO_x mixed oxides, while their oxygen storage capacity (OSC) properties are not only intrinsic to their structures but also limited to their surfaces and by their particle sizes.

1. Introduction

Chlorinated volatile organic compounds (Cl-VOCs) as the main air pollutants are known to be dangerous to the health of humans as well as the environment.[1,2] Catalytic combustion technology is considered to be an efficient way to control Cl-VOC emissions and is extensively used.[3] So far, efforts have been made to investigate all kinds of catalysts including noble metals, zeolites, transition metal oxides, and their mixtures. Although the catalytic activity of noble metals is higher, their industrial applications are very difficult because of high cost and easy deactivation. In order to find cheaper substitutes to noble metal catalysts, the use of various mixed metal oxides has attracted much attention. Mixed oxides such as CeO_2–MnO_x,[4,5] CeO_2–CuO,[6] CeO_2–ZrO_2,[7] CeO_2–CrO_x,[8] and CeO_2–TiO_2 (ref. 9) exhibit excellent catalytic properties for the deep oxidation of Cl-VOCs. Recently, metal oxide crystals with different exposed facets have attracted a lot of attention due to their unique electronic properties and higher reactivity when compared to the bulk phase. For example, Shen *et al.*[10] found that Co_3O_4 nanorods still exhibit exemplary catalytic performances for CO oxidation even at −77 °C. Mai *et al.*[11] also found that the exposed crystalline planes of CeO_2 have an important effect on the ability of a catalyst to release and uptake oxygen as well as its catalytic performance. CeO_2 nanorods with exposed {110} and {100} facets show higher catalytic activity than CeO_2 nanoparticles with primarily exposed {111} facets toward CO oxidation, because the {110} and {100} facets form oxygen vacancies more easily than the stable {111} facet. Similarly, for other oxidation reactions, the structure and morphology of CeO_2 also displays major effects on the catalytic performance. For instance, Dai *et al.*[12] found that in the dichloroethane oxidation reaction, CeO_2 nanorods have higher catalytic activity than CeO_2 nanocubes and CeO_2 nanopolyhedra, and the catalytic activity decreases in the sequence of rod > cube > polyhedron. Chen *et al.*[13] also found that $Ce_{1-x}M_xO_2$ (M = Ti, Zr, and Hf) nanomaterials with exposed {110}, {100}, and {111} facets also display significant morphological effects in ethanol steam reforming reaction and the catalytic performance decreases in the sequence of rod > pipe > cube. The explanation for the better catalytic performance of the metal-doped $Ce_{1-x}M_xO_2$ nanorods is not only related to their exposure to the {110} and {100} facets, but the doping of metals also significantly increases the specific surface area as well as oxygen storage capacity (OSC) of nanomaterials. Recently, CeO_2–MnO_x mixed oxides with high OSC and multiple valences have also attracted much attention, out of which mixed oxides exhibit superior catalytic activity in different reactions like the catalytic reduction of NO_x with NH_3, catalytic decomposition of NO_x, and catalytic oxidation of CO/VOCs at lower temperatures.[14–17] However, their characteristics are still under debate and meaningful to investigate.

In the present study, four CeO_2–MnO_x mixed oxides with different morphologies (rods, plates, polyhedra, and cubes) were synthesized using simple hydrothermal methods and evaluated for the deep oxidation performance of chlorobenzene (CB) as typical Cl-VOCs. The mixed oxides were

Institute of Catalysis, Zhejiang University, Hangzhou 310028, PR China. E-mail: zhourenxian@zju.edu.cn

† These authors contributed equally to this work.

characterized using X-ray diffraction (XRD), X-ray photoelectron spectroscopy (XPS), high-resolution transmission electron microscopy (HR-TEM), N_2 adsorption–desorption, and temperature-programmed reduction (H_2-TPR) techniques. The structural properties of CeO_2–MnO_x catalysts were investigated by XRD Rietveld refinement in order to obtain new information about the morphological effect.

2. Experimental

2.1 Catalysts' preparation

Nanorod and nanocube CeO_2–MnO_x mixed oxides were synthesized by simple hydrothermal methods.[18] Here, 1.16 g $Ce(NO_3)_3 \cdot 6H_2O$ and 0.24 g $Mn(NO_3)_2$ were added into 20 mL deionized water. In a Teflon-lined autoclave, the mixture was slowly added into 60 mL NaOH solution with different concentrations (rod: 4 mol L^{-1}; cube: 6 mol L^{-1}) under vigorous stirring for 30 min and then heated to different temperatures (rod: 100 °C; cube: 180 °C) for 24 h (rod) or 12 h (cube).

The nanoplate CeO_2–MnO_x catalyst was synthesized by a CTAB-assisted hydrothermal method.[19] Here, 2.61 g $Ce(NO_3)_3 \cdot 6H_2O$, 0.54 g $Mn(NO_3)_2$, and 0.73 g CTAB were added into 70 mL distilled water. Afterwards, 10 mL $NH_3 \cdot H_2O$ was slowly added dropwise into the mixed solution under vigorous stirring for 30 min. Then, the mixture was transferred to a Teflon-lined autoclave and heated to 100 °C for 24 h.

The nanopolyhedra CeO_2–MnO_x catalyst was synthesized by the method reported in the literature.[20] Here, 3.47 g $Ce(NO_3)_3 \cdot 6H_2O$, 0.72 g $Mn(NO_3)_2$, and 1.0 g polyvinyl pyrrolidone (PVP; molecular weight = 3000 g mol^{-1}) were added into an autoclave with 40 mL deionized water under vigorous stirring for 30 min. Then, 10 mL $N_2H_4 \cdot H_2O$ was slowly added dropwise into the mixed solution under vigorous stirring for 30 min and heated to 180 °C for 12 h.

The above precipitates were obtained after centrifuging and washing in turn by distilled water and ethanol. The precipitated solids were dried at 60 °C overnight and then calcined in air at 500 °C for 2 h. Afterwards, the samples were sieved to 40–60 meshes (0.3–0.45 mm) and labeled as rod-CeO_2–MnO_x, cube-CeO_2–MnO_x, plate-CeO_2–MnO_x, and polyhedral-CeO_2–MnO_x. The molar ratio of Ce/Mn is 2 : 1 in all the samples.

2.2 Catalysts' characterization

XRD was performed on ARLX'TRA apparatus (Cu Kα radiation, 250 mA, and 40 kV) with 2θ = 10–100°. The XRD Rietveld refinements of the catalysts were performed with Maud software to obtain the microstructure data and the pseudo-Voigt profile function was used to qualitatively and quantitatively analyze the structure.

UV-Raman spectra were recorded on a UV-HR Raman spectrograph apparatus equipped with a laser at 325 nm. The range of the Raman spectra was 100–1000 cm^{-1} and the spectral resolution was 4 cm^{-1}.

The XPS spectra were recorded on a Thermo K-Alpha apparatus equipped with 84 W Al Kα radiation. The binding energies (BEs) of various elements were calibrated using the C 1s peak (284.6 eV).

HR-TEM images were obtained using a TECNAI G220 apparatus at 200 kV. In order to identify the chemical composition, energy dispersive spectrometry (EDS) analysis was performed.

H_2-TPR experiment was carried out on a quartz fixed-bed microreactor equipped with a TCD detector. Before testing, 50 mg of the sample was pretreated in N_2 flow (30 mL min^{-1}) at 200 °C for 30 min and then cooled down to 100 °C. After stabilization, TPR experiments were performed from 100 to 600 °C at a heating rate of 10 °C min^{-1} under 5 vol% H_2/Ar flow (40 mL min^{-1}).

The OSC experiment was carried out on a CHEMBET-3000 apparatus (Quantachrome Co.) equipped with a TCD detector using the pulse injection of CO. Before testing, the samples were pretreated under H_2 flow (30 mL min^{-1}) at 500 °C for 2 h and then cooled down to 400 °C. After stabilization, the gas was switched to He flow (40 mL min^{-1}) for 30 min.

The specific surface areas (S_{BET}) were determined by N_2 adsorption/desorption isotherms at 77 K with Brunauer–Emmett–Teller (BET) theory operating on a Micrometrics TriStar II 2020 analyzer.

2.3 Catalytic activity tests

The catalytic performances of the samples employed in the oxidation of CB were measured in a fixed-bed quartz reactor with 300 mg of catalyst under atmospheric pressure. The reactant gas mixture consisted of CB (1000 ppm) and dry air with a GHSV of 15 000 h^{-1}. The outlet gas was monitored online by a gas chromatograph equipped with TCD and FID detectors. The durability test of the catalysts for DCE degradation was also evaluated. It was exposed to dry air or in the existence of water (2.3 v/v%) or benzene (500 ppm) continuously for a long time.

3. Results and discussion

3.1 Catalytic performance tests

3.1.1 Catalytic activity. The catalytic activity of the CeO_2–MnO_x mixed oxides with different morphologies for CB degradation is shown in Fig. 1A. It is obvious that the catalytic activity is significantly influenced by the morphology of CeO_2–MnO_x catalysts, and rod-CeO_2–MnO_x shows superior catalytic activity for CB destruction than the other three catalysts. It can be seen that the $T_{90\%}$ (temperature with CB conversion of 90%) is the highest for cube-CeO_2–MnO_x (365 °C) and is decreased to different degrees as the morphology of CeO_2–MnO_x catalysts changes from cube to polyhedral, plate, and rod, which is greatly reduced to 303 °C for rod-CeO_2–MnO_x catalyst. Moreover, in the process of CB degradation, no carbon-containing byproducts and polychloride benzene or polychlorobenzene were detected over the samples, which is different from the catalytic behavior of noble metal catalysts.[21,22]

Fig. 1B shows the catalytic performances of rod-CeO_2–MnO_x with different CB concentrations and GHSVs. On one hand, it can be seen that when the GHSV is fixed at 15 000 h^{-1}, the catalytic activity of the catalyst gradually decreases with higher

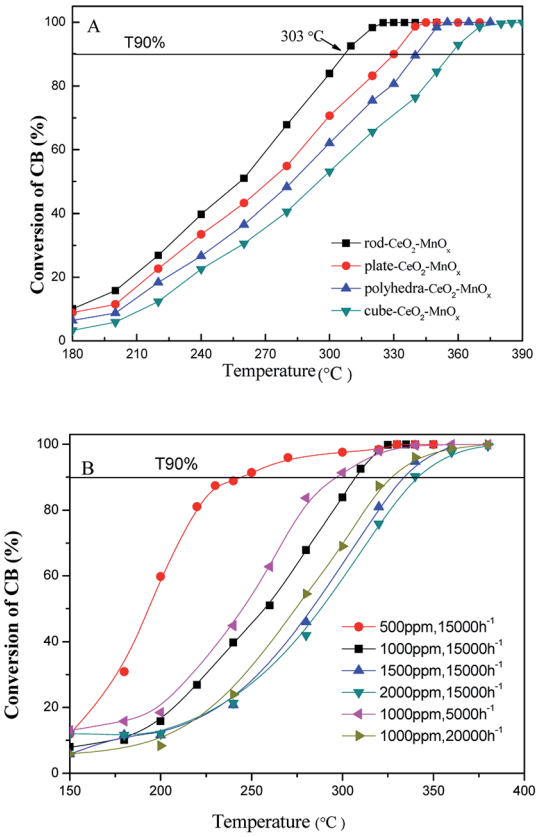

Fig. 1 (A) Catalytic activity of CeO_2–MnO_x catalysts with different morphologies and (B) rod-CeO_2–MnO_x with different CB concentrations and GHSV for CB degradation.

CB concentration; here, $T_{90\%}$ increases by about 100 °C (from 244 °C to 342 °C) as the CB concentration increases from 500 to 2000 ppm. On the other hand, the CB concentration is equal to 1000 ppm and the catalytic performance is evaluated with different GHSVs. The results indicate that higher GHSV leads to poor catalytic performance of rod-CeO_2–MnO_x for CB destruction, which is due to the shorter retention time of CB in the catalyst bed with high GHSV.

3.1.2 Durability of catalysts. In industrial applications, the deactivation of catalysts for Cl-VOCs degradation is an important evaluation index. As shown in Fig. 2, as compared to rod-CeO_2–MnO_x and plate-CeO_2–MnO_x catalysts, CB conversions over the other catalysts decrease in an obvious manner at lower temperatures for the first 5 h at the beginning of the continuous reaction and then tend toward stability. After the reaction system is injected with water steam (2.3 v/v%), CB conversion over rod-CeO_2–MnO_x catalyst decreases slightly and it increases slightly over the other catalysts; however, their catalytic activities return to the original level after cutting off the water steam. Generally, during the degradation of Cl-VOCs, the catalysts may be partially or even completely deactivated because the carbon deposits and/or the chlorine species are strongly adsorbed on the surface of the catalysts at lower temperatures. Therefore, after being treated in a stream of dry air at 400 °C for 0.5 h, the decreased activities of the CeO_2–MnO_x mixed oxides are

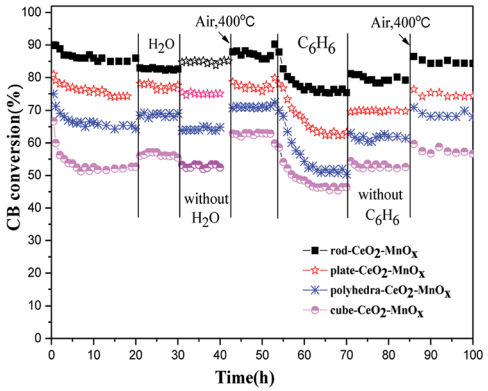

Fig. 2 Durability test of CeO_2–MnO_x catalysts with different morphologies for CB degradation in dry air, H_2O (2.3 v/v%), or C_6H_6 (500 ppm) at 310 °C.

completely recovered. According to the literature,[23] on one hand, the presence of H_2O can decrease the chloride and carbon contents on the used samples, which is beneficial to improve the catalytic performances, and on the other hand, the competitive adsorption between H_2O and CB would impair the catalytic activity for CB destruction. For rod-CeO_2–MnO_x, the reduced CB conversion indicates that the presence of H_2O severely inhibits CB oxidation because of the easy competitive adsorption on the active sites than the reactant molecules (*i.e.*, CB). Further, for the other three catalysts, the addition of H_2O mainly promotes the movement of Cl species and carbonaceous deposits from the surface of the catalysts, yielding improved catalytic performances. Moreover, the complete recovery of the catalytic activity with the treatment of dry air at 400 °C is mainly due to the fact that dry air could remove the carbon deposits and/or chlorine species that get strongly adsorbed on the surface of the catalysts at lower temperatures during the degradation of Cl-VOCs.

In addition, the effect of other VOCs on the catalytic activities of CeO_2–MnO_x for CB degradation is also evaluated. As shown in Fig. 2, after a certain concentration of benzene (500 ppm) was injected into the reaction system, CB conversions over the CeO_2–MnO_x catalysts decrease in an obvious manner, and the catalytic activity of all the four catalysts could not recover after removing C_6H_6. However, after being treated in dry air at 400 °C for 30 min, the decreased activities of CeO_2–MnO_x catalysts are completely recovered. According to the literature,[24] the presence of C_6H_6 could result in strong competitive adsorption and oxidation of C_6H_6 on the active sites of catalysts for CB destruction and increase the carbon content on the used samples, which dramatically decreases the catalytic activity of CeO_2–MnO_x catalysts.

3.2 Structural properties of catalysts

3.2.1 XRD and XRD Rietveld analyses. Efforts have been made on the XRD Rietveld refinement by using Maud software to obtain the microstructural information of CeO_2–MnO_x mixed oxides with different morphologies. XRD and Rietveld XRD patterns of the CeO_2–MnO_x mixed oxides are shown in Fig. 3,

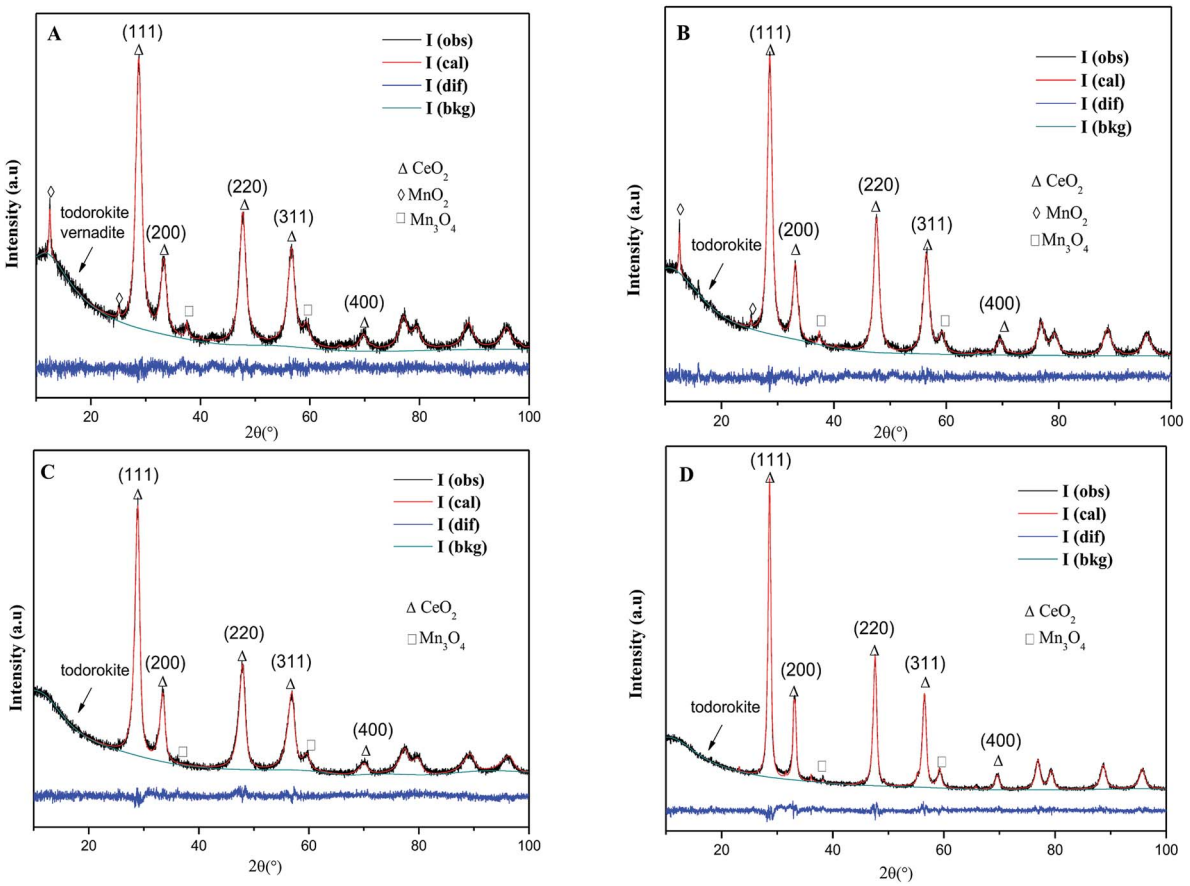

Fig. 3 XRD and Rietveld XRD patterns of CeO_2–MnO_x catalysts with different morphologies: (A) rod-CeO_2–MnO_x, (B) plate-CeO_2–MnO_x, (C) polyhedra-CeO_2–MnO_x, and (D) cube-CeO_2–MnO_x.

and the related results are listed in Table 1. The characteristic diffraction peaks of CeO_2 (S.G.: $Fm\bar{3}m$) with a fluorite structure are observed in all the samples, but the rod-MnO_x–CeO_2 shows the broadest peak as compared to the other three catalysts, indicating that the particle size of the rod-MnO_x–CeO_2 is smaller. Except for the characteristic peaks of CeO_2, the diffraction peaks of Mn_3O_4 (S.G.: $I4_1/amd$) appeared at $2\theta =$ ~36.3° and 59.9° in all the catalysts, and the diffraction peak of MnO_2 (S.G.: $I4/m$) appeared at $2\theta = 12.5°$ in rod-MnO_x–CeO_2 and plate-MnO_x–CeO_2 are also observed.[25,26] In addition, it is noteworthy that two new phases (todorokite and vernadite) with a special tunnel-like structure, which are usually ignored, are found in the MnO_x–CeO_2 mixed oxides. The diffraction peak assigned to the new phase appears at lower than 20°. The

Table 1 Structural parameters deduced from Rietveld refinement of the XRD patterns for CeO_2–MnO_x catalysts with different morphologies

Samples	Component	S.G.	a/Å	b/Å	c/Å	CeO_2 crystallite (Å)	R.M.S. microstrain/CeO_2
Rod-CeO_2–MnO_x	CeO_2	$Fm\bar{3}m$	5.376	—	—		
	MnO_2	$I4/m$	10.049	—	2.371	{111}:79.10	{111}:0.005
	Mn_3O_4	$I4_1/amd$	5.765	—	9.450	{100}:78.49	{100}:0.013
	Todorokite	$P2/m$:b	7.905	2.237	10.535	{110}:84.77	{110}:0.008
	Vernadite	$I4/m$	9.445	—	2.855		
Plate-CeO_2–MnO_x	CeO_2	$Fm\bar{3}m$	5.381	—	—	{111}:86.10	{111}:0.003
	MnO_2	$I4/m$	10.049	—	2.371	{100}:80.49	{100}:0.009
	Mn_3O_4	$I4_1/amd$	5.765	—	9.450	{110}:82.75	{110}:0.006
	Todorokite	$P2/m$:b	7.916	2.248	10.533		
Polyhedra-CeO_2–MnO_x	CeO_2	$Fm\bar{3}m$	5.389	—	—	{111}:105.62	{111}:0.004
	Mn_3O_4	$I4_1/amd$	5.765	—	9.450	{100}:103.79	{100}:0.005
	Todorokite	$P2/m$:b	7.989	2.253	10.563	{110}:113.74	{110}:0.003
Cube-CeO_2–MnO_x	CeO_2	$Fm\bar{3}m$	5.398	—	—	{111}:116.62	{111}:0.004
	Mn_3O_4	$I4_1/amd$	5.765	—	9.450	{100}:107.73	{100}:0.004
	Todorokite	$P2/m$:b	7.934	2.247	10.559	{110}:110.29	{110}:0.003

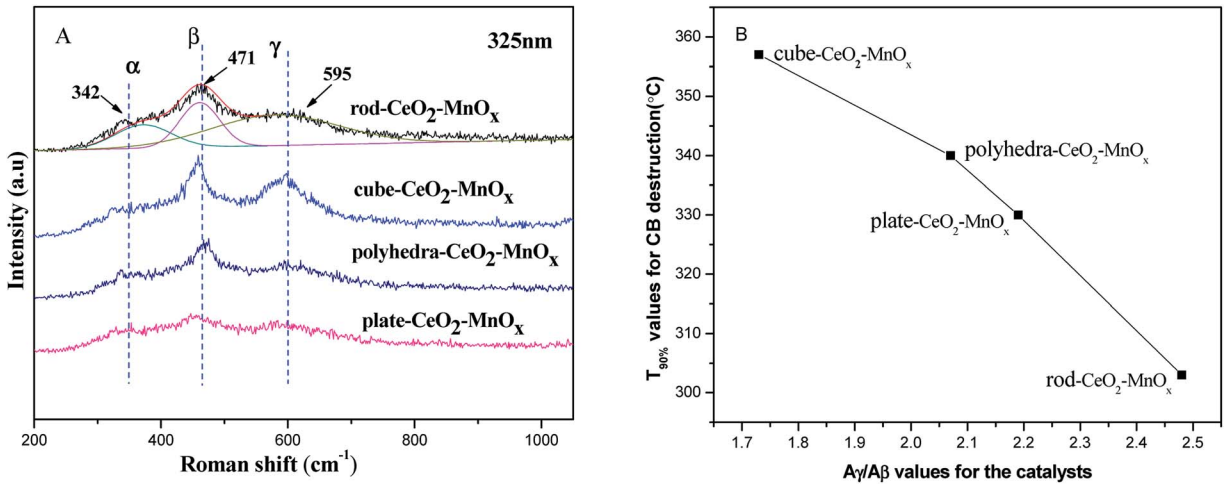

Fig. 4 UV-Raman spectra (A) and $T_{90\%}$ values *versus* A_γ/A_β ratios (B) of CeO_2–MnO_x catalysts with different morphologies.

todorokite phase (S.G.: *P*2/*m*:*b*) exists in all the MnO_x–CeO_2 mixed oxides, while the vernadite phase (S.G.: *I*4/*m*) only exists in rod-MnO_x–CeO_2. According to the intensity of the diffraction peak at lower than 20°, this means that the content of the new phases is the highest in rod-MnO_x–CeO_2 and the lowest in cube-CeO_2–MnO_x, which is consistent with the activity of the catalysts. Therefore, the result probably implies that the existence of both todorokite and vernadite phases with a special tunnel-like structure can promote the catalytic performance for CB oxidation. On the other hand, the results of Rietveld refinements also suggest that for CeO_2–MnO_x mixed oxides, CeO_2 and MnO_x crystallites are highly dispersed within each other, indicating that Mn^{3+} or Mn^{2+} cannot enter into the CeO_2 lattice to form $CeMnO_x$ solid solution, which is considered in the literature.[4,5] As shown in Table 1, the lattice microstrains of CeO_2 on different facets in rod-CeO_2–MnO_x are bigger than those in the other three catalysts. In particular, for the {110} and {100} facets, the lattice microstrain of rod-CeO_2–MnO_x is the highest and apparently higher than those of both polyhedra-CeO_2–MnO_x and cube-CeO_2–MnO_x. The lattice microstrain decreases in the following sequence: rod-CeO_2–MnO_x > plate-CeO_2–MnO_x > polyhedra-CeO_2–MnO_x > cube-CeO_2–MnO_x. The microstrain is generated due to lattice distortion and defects, which is favorable to forming more oxygen vacancies. Thus, the increased oxygen vacancy concentration would facilitate the process in which the active oxygen species existing on the subsurface migrate toward the surface of the catalysts, resulting in increasing catalytic activity. Moreover, the size of the CeO_2 crystallites (Table 1) can also explain the growth characteristics of the exposed crystal planes; for example, the exposed {100} (78.49 Å) and {110} (84.77 Å) planes of rod-CeO_2–MnO_x grow on the orientated attachment with a [110] growth direction. Further, this is in agreement with the results of the HRTEM (discussed below).

3.2.2 UV-Raman results. The UV-Raman spectra provided information about the vibration of oxygen lattices. The UV-Raman profiles and $T_{90\%}$ values *versus* A_γ/A_β ratios of CeO_2–MnO_x mixed oxides with different morphologies are shown in Fig. 4A and B, respectively. In Fig. 4A, three main peaks appearing at 342 cm^{-1} (α), 471 cm^{-1} (β), and 595 cm^{-1} (γ) can be observed, which is the same as that in the literature.[27,28] The weak peak α is assigned to an intermediate phase named as t″, between t′ and cubic CeO_2, which is metastable. Peak β is related to the F_{2g} vibration mode of the cubic fluorite-type structure. The shift in the broad F_{2g} band implies that the ceria species apparently possess a distorted structure, which can cause the generation of oxygen vacancies in ceria.[29] Peak γ is assigned to the oxygen vacancies in CeO_2, which is favorable to the defective structure in CeO_2. Usually, the intensity ratio (A_γ/A_β) of the peaks between 595 cm^{-1} and 471 cm^{-1} is calculated to show the relative oxygen vacancies concentration. From Fig. 4B, rod-CeO_2–MnO_x shows a much higher A_γ/A_β ratio (2.49), while the A_γ/A_β ratio for cube-CeO_2–MnO_x is only 69% of that for rod-CeO_2–MnO_x. The A_γ/A_β ratio decreases in the following order: rod-CeO_2–MnO_x (2.49) > plate-CeO_2–MnO_x (2.22) > polyhedra-CeO_2–MnO_x (2.07) > cube-CeO_2–MnO_x (1.72). This suggests that the oxygen vacancies concentration in the rod-CeO_2–MnO_x catalyst is more than that of the other three catalysts, which is in good agreement with the XRD Rietveld refinement results. The oxygen vacancies with high concentration would promote the diffusion of active oxygen species from bulk phase to the surface of the catalysts, which promotes the catalytic activity of CeO_2–MnO_x mixed oxides for CB oxidation.

3.2.3 XPS results. The XPS data of the CeO_2–MnO_x mixed oxides with different morphologies are given in Table 2. As shown in Table 2, rod-CeO_2–MnO_x has a higher relative concentration of Ce^{3+} in Ce than the other catalysts and the ratio of Ce^{3+}/Ce^{4+} is in the sequence of rod-CeO_2–MnO_x (0.48) > plate-CeO_2–MnO_x (0.42) > polyhedra-CeO_2–MnO_x (0.36) > cube-CeO_2–MnO_x (0.28). Generally, there are some direct relationships between the presence of Ce^{3+} and the generation of oxygen vacancies. Thus, the above result is also in good agreement with the UV-Raman results. As for the Mn element, the ratio of Mn/Ce in rod-CeO_2–MnO_x is much higher than its theoretical value (0.50) and the content of MnO_2 is also higher than that in the other catalysts. The value of Mn/Ce decreases in

Table 2 Surface elemental composition and the oxidation state of Ce and Mn measured by XPS

	Surface composition (at%)			Mn distribution (at%)			O distribution (at%)			
Samples	Ce 3d	Mn 2p	O 1s	Mn^{4+}	Mn^{3+}	Mn^{2+}	O_{latt}	O_{sur}	Mn/Ce	Ce^{3+}/Ce^{4+}
Rod-CeO_2–MnO_x	16.12	11.25	72.63	6.04	1.49	3.56	43.47	29.16	0.70	0.48
Plate-CeO_2–MnO_x	19.09	9.85	71.06	4.89	1.40	3.45	44.71	26.35	0.52	0.42
Polyhedra-CeO_2–MnO_x	23.45	8.66	67.89	4.21	2.93	1.42	46.75	21.14	0.37	0.36
Cube-CeO_2–MnO_x	26.79	7.72	65.49	4.74	2.08	0.84	48.37	17.12	0.29	0.28

the order of rod-CeO_2–MnO_x (0.70) > plate-CeO_2–MnO_x (0.52) > polyhedra-CeO_2–MnO_x (0.37) > cube-CeO_2–MnO_x (0.29). This result indicates that Mn enrichment and the presence of more Mn^{4+} species on the surface of the catalysts would increase the catalytic performances of CeO_2–MnO_x mixed oxides for Cl-VOC oxidation. Moreover, there are more Mn^{2+} species in rod-CeO_2–MnO_x and plate-CeO_2–MnO_x catalysts, which is related to the generation of oxygen vacancies owing to retaining the charge neutrality in the oxides.[30] Thus, the reduction of Ce^{4+} to Ce^{3+} may also be promoted due to the presence of the redox cycle of Mn^{2+}–Mn^{4+}, which would promote the migration of lattice oxygen as well as the catalytic performance. On the other hand, it suggests that there is a stronger interaction between MnO_x and rod/plate-CeO_2 species in rod-CeO_2–MnO_x and plate-CeO_2–MnO_x, which is beneficial toward the formation of more Mn^{4+} and Ce^{3+} species, further promoting the deeper oxidation of Cl-VOCs. In addition, with respect to the O element, from Table 2, there are two different oxygen species:[31,32] lattice oxygen (O_{latt}) and surface oxygen species (O_{sur}) such as hydroxyl, carbonate species, adsorbed oxygen (O^-/O_2^{2-}), and adsorbed water on the surface. It is noteworthy that the value of O_{sur}/O_{latt} decreases in the sequence of rod-CeO_2–MnO_x (0.67) > plate-CeO_2–MnO_x (0.59) > polyhedra-CeO_2–MnO_x (0.45) > cube-CeO_2–MnO_x (0.35), indicating that high O_{sur} species content on the surface of CeO_2–MnO_x mixed oxides would promote the deeper oxidation of CB.

3.3 Morphologies of catalysts

As shown in Fig. 5, CeO_2–MnO_x mixed oxides with different morphologies were successfully synthesized. Fig. 5A and B show that rod-CeO_2–MnO_x catalyst is a long rod-like nanoparticle with dimensions of (10.5 ± 1.6) nm × (50–200) nm, clearly showing three different lattice plane spacings ascribed to the {111} (0.31 nm), {002} (0.28 nm), and {110} (0.19 nm) facets. Interestingly, when observed and calculated along the long attitudinal axis, the plane-intersecting angle of 45° further proves that rod-CeO_2–MnO_x mainly exposes the {100} (0.26 nm) facet and preferentially grows along the direction of the {110} facet.[33] Fig. 5C and D reveal that plate-CeO_2–MnO_x is a rhombic plate with a diameter of 18 nm and thickness of ~4 nm, exposing two facets, namely, {111} (0.31 nm) and {200} (0.27 nm). From Fig. 5E, polyhedra-CeO_2–MnO_x is an irregular hexagonal nanoparticle, which comprises truncated octahedra with an average size of about 20 ± 1.5 nm. From Fig. 5F, the polyhedra-CeO_2–MnO_x shows {200}, {111}, and {220} facets corresponding to the interplanar spacings of 0.26, 0.33, and

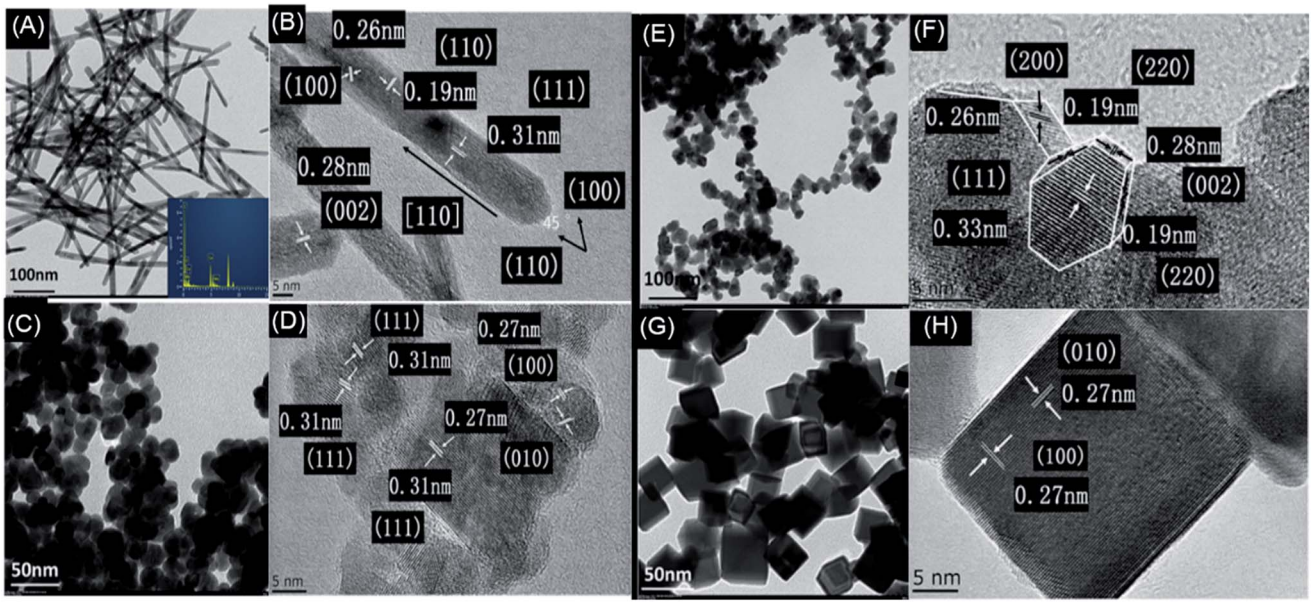

Fig. 5 TEM and HRTEM images of CeO_2–MnO_x catalysts with rod (A and B), plate (C and D), polyhedral (E and F) and cube (G and H) morphologies.

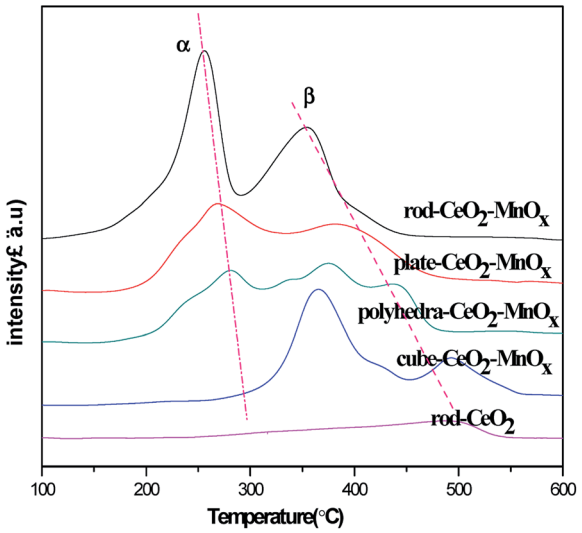

Fig. 6 H_2-TPR profiles of CeO_2–MnO_x catalysts with different morphologies.

0.19 nm, respectively, indicating that it exposes the {111} and {100} facets.[34] From Fig. 5G and H, it can be seen that cube-CeO_2–MnO_x is a more uniform cube block with a size of 20–25 nm and has a bigger particle size than the others. Further, it is only enclosed by the {100} facet. Generally, the exposed crystal face plays an important role in the catalytic performance of the catalysts. The {111} facet is much more stable than the {110} and {100} facets with a higher surface energy; the former is inactive as compared to the latter facets. Therefore, rod-CeO_2–MnO_x that mainly exposed the {100} facet exhibits higher catalytic activity for CB degradation. Although cube-CeO_2–MnO_x is enclosed by the {100} facets, it has a bigger particle size and lower concentration of oxygen vacancies, resulting in a dramatic decrease in the catalytic activity for CB oxidation in the low-temperature range. Moreover, the chemical composition is also identified by high-resolution EDS. As shown in Fig. 5A, manganese and cerium species are detected in rod-CeO_2–MnO_2, implying the existence of Mn species on the surface of CeO_2.

3.4 Redox properties of catalysts

The redox properties of CeO_2–MnO_x mixed oxides with different morphologies were tested by H_2-TPR, and the related profiles are shown in Fig. 6. As shown in Fig. 6, for pure rod-CeO_2, the reduction peak below 600 °C is rather weak, which corresponds to the reduction of two kinds of oxygen species that are present on the surface and subsurface. It implies that CeO_2 represents poor oxidation performance at lower temperatures. For CeO_2–MnO_x mixed oxides, except for polyhedra-CeO_2–MnO_x, two obvious reduction peaks (α and β) are observed, which belong to the reduction of MnO_x species and oxygen species on the surface/subsurface of CeO_2. Generally, at lower temperatures, peak α corresponds to the reduction of MnO_x species that are highly dispersed and interact with ceria. As for peak β, it may be attributed to the combined reduction of Mn_2O_3 to MnO or MnO_x species with larger particles and surface/subsurface oxygen species of ceria.[35–37] Further, for polyhedra-CeO_2–MnO_x, the profile of H_2-TPR shows multiple peaks, which may be related to more exposed planes and heterogeneous polyhedral particles.[38] Among them, rod-CeO_2–MnO_x catalyst has the best reducibility, while cube-CeO_2–MnO_x catalyst has the worst. The reducibility of mixed oxides decreases in the following order: rod-CeO_2–MnO_x > plate-CeO_2–MnO_x > polyhedra-CeO_2–MnO_x > cube-CeO_2–MnO_x. However, as reported in the literature,[39] the temperatures for the reduction of pure MnO_x are much higher than those for MnO_x species in CeO_2–MnO_x mixed oxides. This implies that there is a strong interaction between CeO_2 and MnO_x, which promotes the mobility of active oxygen species and further enhances the catalytic activity for CB oxidation.

3.5 OSC properties of catalysts

The OSC value has a substantial impact on the catalytic performance for deep oxidation. Thus, the OSC measurement of CeO_2–MnO_x mixed oxides with different morphologies was carried out at 400 °C, and the data is listed in Table 3. The OSC value of rod-CeO_2–MnO_x (574 μmol O_2 g^{-1}) is the highest and much larger than that of cube-CeO_2–MnO_x (106 μmol O_2 g^{-1}). The OSC value decreases in the following order: rod-CeO_2–MnO_x > plate-CeO_2–MnO_x > polyhedra-CeO_2–MnO_x > cube-CeO_2–MnO_x, which is consistent with the results of the catalytic activity test. According to the literature,[40] the OSC values of CeO_2-based mixed oxides are intrinsic to their structures. A more homogeneous structure would create more oxygen that would result in an increase in the OSC value. Moreover, it is worth noting that the variation of the OSC value is consistent with those of their BET surface area (S_{BET}) and OSC/S_{BET} values, suggesting that the OSC value of the catalysts is also limited to its surface and particle size. As the BET surface area dramatically decreases, the available oxygen species on the surface also decline, which leads to a decrease in the OSC value. In addition, for rod-CeO_2–MnO_x and plate-CeO_2–MnO_x, their OSC/S_{BET} values are also higher than the theoretical ones (calculated

Table 3 Exposed facets, OSCs, and surface areas of CeO_2–MnO_x catalysts with different morphologies

Samples	Exposed facets	OSC (μmol O_2 g^{-1})	S_{BET} (m^2 g^{-1})	OSC/S_{BET} (μmol O_2 m^{-2})	Calculated OSC (μmol O_2 m^{-2})[a]
Rod-CeO_2–MnO_x	{100} + {110}	574	75.6	7.5	4.9[b]
Plate-CeO_2–MnO_x	{200} + {111}	479	70.8	6.8	6.6
Polyhedra-CeO_2–MnO_x	{100} + {111}	256	48.1	5.3	6.6[b]
Cube-CeO_2–MnO_x	{100}	106	33.7	3.1	5.7

[a] Calculated according to the theoretical OSC of the {100}, {110}, and {111} facets for CeO_2.[41] [b] Assumption: balanced distribution of oxygen species on different facets.[42]

OSCs). This result indicates that the mobility of active oxygen species in rod-CeO_2–MnO_x and plate-CeO_2–MnO_x is better, which increases the migration rate of bulk oxygen toward the surface, thereby improving the catalytic activity for CB oxidation.

4. Conclusion

Four CeO_2–MnO_x mixed oxides with different morphologies were prepared by simple hydrothermal methods and characterized using XRD, XPS, HRTEM, N_2 adsorption–desorption, and H_2-TPR techniques. Rod-CeO_2–MnO_x mainly exposes the {100} facet and preferentially grows along the {110} facet direction. Plate-CeO_2–MnO_x is dominated by the {111} facet and polyhedra-CeO_2–MnO_x exposes the {111} and {100} facets, while cube-CeO_2–MnO_x with a bigger particle size is only enclosed by the {100} facet. The XRD Rietveld refinement results show that CeO_2 and MnO_x in the CeO_2–MnO_x mixed oxides are highly dispersed with respect to each other. Two new phases of both todorokite and vernadite with a special tunnel-like structure are found. The todorokite phase (S.G.: *P*2/*m*:*b*) exists in all the MnO_x–CeO_2 mixed oxides, while the vernadite phase (S.G.: *I*4/*m*) only exists in rod-MnO_x–CeO_2. Moreover, the lattice microstrain generated from the lattice distortion and defects decreases in the following order: rod-CeO_2–MnO_x > plate-CeO_2–MnO_x > polyhedra-CeO_2–MnO_x > cube-CeO_2–MnO_x, which is consistent with their OSC values. The results of UV-Raman and XPS spectra reveal that rod-CeO_2–MnO_x and plate-CeO_2–MnO_x have higher concentrations of Ce^{3+} and Mn^{2+} as compared to the other catalysts, particularly when compared to cube-CeO_2–MnO_x, which is favorable for the promotion of lattice oxygen mobility and further enhancing the catalytic activity for Cl-VOCs oxidation. Moreover, Mn enrichment and more Mn^{4+} species on the CeO_2–MnO_x surface are also beneficial toward improved catalytic activity. The H_2-TPR and OSC results show that the catalytic performance of the catalysts can be enhanced because CeO_2 and MnO_x strongly interact with each other, while their OSC properties are not only intrinsic to their structures but also limited to their surfaces and by their particle sizes.

Conflicts of interest

There are no conflicts to declare.

Acknowledgements

The financial supports from the National Key Research and Development Program of China (2016YFC0204300) and the Natural Science Foundation of China (No. 21477109) are gratefully acknowledged.

References

1 E. C. Moretti, *Practical Solutions for Reducing Volatile Organic Compounds and Hazardous Air Pollutants*, 2001.
2 S. Maghsoodi, J. Towfighi, A. Khodadadi and Y. Mortazavi, *Chem. Eng. J.*, 2013, **215–216**, 827–837.
3 Q. G. Dai, X. Y. Wang and G. Z. Lu, *Appl. Catal., B*, 2008, **81**, 192–202.
4 X. Y. Wang, L. Ran, Y. Dai, Y. J. Lu and Q. G. Dai, *J. Colloid Interface Sci.*, 2014, **426**, 324–332.
5 X. Y. Wang, Q. Kang and D. Li, *Appl. Catal., B*, 2009, **86**, 166–175.
6 X. D. Ma, X. Feng, X. He, H. W. Guo, L. Lv, J. Guo, H. Q. Cao and T. Zhou, *Microporous Mater.*, 2012, **158**, 214–218.
7 B. de Rivas, R. López-Fonseca, M. Á. Gutiérrez-Ortiz and J. I. Gutiérrez-Ortiz, *Appl. Catal., B*, 2011, **101**, 317–325.
8 P. Yang, Z. N. Shi, S. S. Yang and R. X. Zhou, *Chem. Eng. Sci.*, 2015, **126**, 361–369.
9 Z. N. Shi, P. Yang, F. Tao and R. X. Zhou, *Chem. Eng. J.*, 2016, **295**, 99–108.
10 X. W. Xie, Y. Li, Z. Q. Liu, H. Masatake and W. J. Shen, *Nature*, 2009, **458**, 746–748.
11 H. X. Mai, L. D. Sun, Y. W. Zhang, R. Si, W. Feng, H. P. Zhang, H. C. Liu and C. H. Yan, *J. Phys. Chem. B*, 2005, **109**, 24380–24385.
12 Q. Dai, H. Huang, Y. Zhu, W. Deng, S. Bai, X. Wang and G. Lu, *Appl. Catal., B*, 2012, **117–118**, 360–368.
13 W. T. Chen, K. B. Chen, M. F. Wang, S. F. Weng, C. S. Lee and M. C. Li, *Chem. Commun.*, 2010, **46**, 3286–3288.
14 G. Qi, R. T. Yang and R. Chang, *Appl. Catal., B*, 2004, **51**, 93–106.
15 P. Zhang, H. Lu, Y. Zhou, L. Zhang, Z. Wu, S. Yang, H. Shi, Q. Zhu, Y. Chen and S. Dai, *Nat. Commun.*, 2015, **6**, 8446.
16 F. Arena, B. Gumina, A. F. Lombardo, C. Espro, A. Patti, L. Spadaro and L. Spiccia, *Appl. Catal., B*, 2015, **162**, 260–267.
17 Z. Wang, G. Shen, J. Li, H. Liu, Q. Wang and Y. Chen, *Appl. Catal., B*, 2013, **138**, 253–259.
18 H. Mai, L. Sun, Y. Zhang, R. Si, W. Feng, H. Zhang, H. Liu and C. Yan, *J. Phys. Chem. B*, 2005, **109**, 24380–24385.
19 C. Pan, D. Zhang and L. Shi, *J. Solid State Chem.*, 2008, **181**, 298–1306.
20 F. Lu, F. Meng, L. Wang, J. Luo and Y. Sang, *Mater. Lett.*, 2012, **73**, 154–156.
21 M. Kułażyński, J. G. van Ommen, J. Trawczyński and J. Walendziewski, *Appl. Catal., B*, 2002, **36**, 239–247.
22 H. Windawi and Z. C. Zhang, *Catal. Today*, 1996, **30**, 99–105.
23 C. E. Hetrick, F. Patcas and M. D. Amiridis, *Appl. Catal., B*, 2011, **101**, 622–628.
24 T. Fei, S. S. Yang, P. Yang, Z. N. Shi and R. X. Zhou, *J. Rare Earths*, 2016, **34**, 381–389.
25 Z. Chen, F. Wang, H. Li, Q. Yang, L. Wang and X. Li, *Ind. Eng. Chem. Res.*, 2012, **51**, 202–212.
26 G. Park, L. Bartolome, K. G. Lee, S. J. Lee, D. H. Kim and T. J. Park, *Nanoscale*, 2012, **4**, 3879–3885.
27 L. Li, F. Chen, J.-Q. Lu and M.-F. Luo, *J. Phys. Chem. A*, 2011, **15**, 7972–7977.
28 T. Taniguchi, T. Watanabe, N. Sugiyama, A. K. Subramani, H. Wagata, N. Matsushita and M. Yoshimura, *J. Phys. Chem.*, 2009, **113**, 19789–19793.
29 P. Sudarsanam, K. Kuntaiah and B. M. Reddy, *New J. Chem.*, 2014, **38**, 5991–6001.
30 P. Sudarsanam, B. Hillary, M. H. Amin, S. B. A.Hamid and S. K. Bhargava, *Appl. Catal., B*, 2016, **185**, 213–224.

31 H. C. Yao and Y. F. Yu Yao, *J. Catal.*, 1984, **86**, 254–265.
32 H. Y. Chen, A. Sayari, A. Adnot and F. Larach, *Appl. Catal., B*, 2001, **32**, 195–204.
33 Z. Zhang, C. Hu, Y. Xiong, R. Yang and Z. L. Wang, *Nanotechnology*, 2007, **18**, 465–504.
34 Z. L. Wang and X. Feng, *J. Phys. Chem. B*, 2003, **107**, 13563–13566.
35 D. Terribile, A. Trovarelli, C. De Leitenburg, A. Primavera and G. Dolcetti, *Catal. Today*, 1999, **47**, 133–140.
36 X. Tang, Y. Li, X. Huang, Y. Xu, H. Zhu, J. Wang and W. Shen, *Appl. Catal., B*, 2006, **62**, 265–273.
37 D. Delimaris and T. Ioannides, *Appl. Catal., B*, 2008, **84**, 303–312.
38 H. J. Li, G. S. Qi, T. Na, X. J. Zhang, W. Li and W. J. Shen, *Catal. Sci. Technol.*, 2011, **1**, 1677–1682.
39 J. L. Ayastuy, E. Fernández-Puertas, M. P. González-Marcos and M. A. Gutiérrez-Ortiz, *Int. J. Hydrogen Energy*, 2012, **37**, 7385–7397.
40 H. Vidal, J. Kaspar, M. Pijolat, G. Colon, S. Bernal, A. Cordón, V. Perrichon and F. Fally, *Appl. Catal., B*, 2001, **30**, 75–85.
41 E. López-Navarrete, A. Caballero, A. R. González-Elipe and M. Ocaña, *J. Eur. Ceram. Soc.*, 2004, **24**, 3057–3062.
42 J. R. McBride, K. C. Hass, B. D. Poindexter and W. H. Weber, *J. Appl. Phys.*, 1994, **76**, 2435–2441.